Pure appl. geophys. 160 (2003) 851–868
0033–4553/03/060851–18

Pure and Applied Geophysics

Failure Mode and Spatial Distribution of Damage in Rothbach Sandstone in the Brittle-ductile Transition

PIERRE BÉSUELLE,[1] PATRICK BAUD,[2]
and TENG-FONG WONG[3]

Abstract—To elucidate the spatial complexity of damage and evolution of localized failure in the transitional regime from brittle faulting to cataclastic ductile flow in a porous sandstone, we performed a series of triaxial compression experiments on Rothbach sandstone (20% porosity). Quantitative microstructural analysis and X-ray computed tomography (CT) imaging were conducted on deformed samples. Localized failure was observed in samples at effective pressures ranging from 5 MPa to 130 MPa. In the brittle faulting regime, dilating shear bands were observed. The CT images and stereological measurements reveal the geometric complexity and spatial heterogeneity of damage in the failed samples. In the transitional regime (at effective pressures between 45 MPa and 130 MPa), compacting shear bands at high angles and compaction bands perpendicular to the maximum compression direction were observed. The laboratory results suggest that these complex localized features can be pervasive in sandstone formations, not just limited to the very porous aeolian sandstone in which they were first documented. The microstructural observations are in qualitative agreement with theoretical predictions of bifurcation analyses, except for the occurrence of compaction bands in the sample deformed at effective pressure of 130 MPa. The bifurcation analysis with the constitutive model used in this paper is nonadequate to predict compaction band formation, may be due to the neglect of bedding anisotropy of the rock and multiple yield mechanisms in the constitutive model.

Key words: Damage, sandstone, brittle-ductile transition, microscopy, X-ray computed tomography, bifurcation theory.

1. Introduction

In porous sandstones, a transition in failure mode from brittle faulting to cataclastic flow occurs as effective pressure increases. Under a relatively low pressure the differential stress attains a peak before it undergoes strain softening; the failure of sample occurs by shear localization. On the other hand, under high confinement the

[1] Ecole Normale Supérieure, Laboratoire de Géologie, Paris, France. Now, Laboratoire Sols, Solides, Structures (CNRS, UJF, INPG), BP53, 38041 Grenoble Cedex 9, France. E-mail: Pierre.Besuelle@inpg.fr
[2] E.O.S.T., Laboratoire de Physique des Roches, 5 rue René Descartes, 67084 Strasbourg Cedex, France.
[3] State University of New York at Stony Brook, Department of Geosciences, Stony Brook, NY 11794-2100, U.S.A.

sample strain hardens and fails by delocalized cataclastic flow (PATERSON, 1978; WONG *et al.*, 1997).

Some intriguing field observations and new theoretical analysis have focused on the mechanical behavior in the *transitional* regime: historically the failure mode in this regime is described as a mosaic of conjugate shear bands and yet recent field and experimental observations indicate the development of discrete compaction bands orthogonal to the maximum compressive stress σ_1 (MOLLEMA and ANTONELLINI, 1996; OLSSON, 1999). This agrees with recent bifurcation analyses (ISSEN and RUDNICKI, 2000) which predict a continuous transition of the localization mode from extension bands (parallel to σ_1) to compaction bands as a function of the constitutive parameters that characterize porosity change and frictional dependence of plastic yield. In the transitional regime between these two failure modes, localization develops by shear bands (inclined with respect to σ_1 at angles ranging from 0^o to 90^o) which may be dilating or compacting (BÉSUELLE, 2001).

Since they can act as barriers to fluid transport and influence the stress field and strain partitioning in sedimentary formations, it is important to gain a fundamental understanding of the extent of and conditions under which these localized compactant structures would occur. Preliminary microstructural studies (DIGIOVANNI *et al.*, 2000; WONG *et al.*, 2001) have shown that such complex development of localization can occur in sandstones with porosities ranging from 13% to 28%. Acoustic emission locations (OLSSON and HOLCOMB, 2000) have also mapped out the three-dimensional complexity of the localization development in the Castlegate sandstone (with 28% porosity). In this study we systematically conducted mechanical tests on the Rothbach sandstone (with a porosity of 20%), and characterized the spatial heterogeneity in porosity change and damage using X-ray computed tomography (CT) imaging and stereological measurements on optical micrographs, respectively. These two types of complementary measurements provide useful insights into the geometric complexity and micromechanics associated with the development of compaction and shear bands in the brittle-ductile transition.

2. Experimental Procedure

Rothbach sandstone from the Vosges mountains in eastern France was used is this study. Our samples came from the same block studied by DAVID *et al.* (1994) and WONG *et al.* (1997), who have provided the petrophysical description. Cylindrical samples (of diameter 18.1 mm and length 38.1 mm) were cored perpendicular to the sedimentary bedding. The arithmetic mean of connected porosities (measured on each sample) was 20.3%.

The samples were saturated with distilled water and deformed in conventional triaxial conditions following procedures described in detail by BAUD *et al.* (2000). The samples were deformed at a nominal strain rate of 1.3×10^{-5} s^{-1} under fully

drained conditions at a fixed pore pressure of 10 MPa. Each end of the specimen was in contact with a stainless steel spacer with a central hole for fluid inlet. To uniformly distribute the pore fluid, several shallow grooves were made on the spacer surface that was touching the sample. The interfaces with the sample ends were lubricated with a mixture of stearic acid and vaseline (LABUZ and BRIDEL, 1993). Axial strain, differential stress, confining pressure, porosity change as well as acoustic emission activity were monitored during the tests. Axial strain was computed from the displacement of the cell piston measured by an external transducer. Adjustment of a pressure generator kept the pore pressure constant, and the pore volume change was recorded by monitoring the piston displacement of the pressure generator with a displacement transducer. The porosity change was calculated from the ratio of the pore volume change to the initial bulk volume of the sample.

Samples at different stages of deformation were unloaded and retrieved from the pressure vessel for X-ray CT imaging conducted at the Institut Français du Pétrole (Rueil-Malmaison, France). The CT-scanner measures the X-ray attenuation coefficient, which increases with increasing bulk density and atomic number (WELLINGTON and VINEGAR, 1987; ANTONELLINI *et al.*, 1994). In a homogeneous sample the attenuation coefficient is proportional to the bulk density. X-ray radiographs taken from different angles provide a cross-sectional image, and a multiplicity of such slices can be combined to visualize the three-dimensional distribution of density in the deformed specimen. The CT apparatus measured the average X-ray attenuation value in a voxel of $0.2 \times 0.2 \times 1.5$ mm^3. CT imaging has been used to characterize the three-dimensional development of strain localization in sandstone (VINEGAR *et al.*, 1991; BÉSUELLE *et al.*, 2000) and granite (RAYNAUD *et al.*, 1989; KAWAKATA *et al.*, 1999).

Petrographic thin sections of selected samples were also prepared. The deformed samples were first impregnated with epoxy and then sawed along a plane parallel to the axial direction. Using optical microscopy the damage states in the thin sections were characterized quantitatively. For each sample, the spatial distribution of crack density over a total area of 16.3×35.4 mm^2 was characterized. The area centrally located in a thin section was further divided into 10×29 subregions, each of which had an area of 1.63×1.22 mm^2. The reflected images were all acquired at a magnification of 100x. Using stereological techniques (MENÉNDEZ *et al.*, 1996; WU *et al.*, 1999), we counted the number of crack intersections with a test array of 5 parallel lines (spaced at 0.33 mm or 0.24 mm apart) in two orthogonal directions parallel and perpendicular to σ_1, respectively. We denote the linear intercept density (number of crack intersections per unit length) for the array oriented parallel to σ_1 by $P_L^{\parallel}$, and that for the perpendicular array by $P_L^{\perp}$.

For each sample, 290 pairs of stereological parameters ($P_L^{\parallel}$ and $P_L^{\perp}$) were measured to map out the spatial evolution of damage and stress-induced anisotropy.

Since the spatial distribution of damage is approximately axisymmetric in a triaxially compressed sample, the crack surface area per unit volume (S_v) is given by

$$S_v = \frac{\pi}{2} P_L^{\perp} + \left(2 - \frac{\pi}{2}\right) P_L^{\parallel} \tag{1}$$

and the anisotropy of crack distribution (UNDERWOOD, 1970) can be characterized by the parameter

$$\Omega_{23} = \frac{P_L^{\perp} - P_L^{\parallel}}{P_L^{\perp} + (4/\pi - 1) P_L^{\parallel}} \tag{2}$$

that represents the ratio between the surface area of cracks parallel to σ_1 and the total crack surface area.

3. Mechanical Data

The compressive stresses and compactive strains will be taken positive. The maximum and minimum (compressive) principal stresses will be denoted by σ_1 and σ_3, respectively. The pore pressure will be denoted by P_p, and the difference between the confining pressure ($P_c = \sigma_2 = \sigma_3$) and pore pressure will be referred to as "effective pressure."

The mechanical behavior and failure mode of porous sandstones have several common attributes (WONG *et al.*, 1997). At low pressures, failure involves dilatancy and faulting, with a failure envelope described by the Coulomb surface, with positive pressure dependence. At high pressures, the samples fail by strain hardening and shear-enhanced compaction. The compactive yield is characterized by an elliptical cap that has negative pressure dependence. The brittle-ductile transition occurs in the regime where these two envelopes meet.

Guided by the mechanical data of WONG *et al.* (1997) on Rothbach sandstone, we performed 15 triaxial experiments at effective pressures ranging from 5 to 130 MPa to capture the evolution of the failure modes in the transitional regime. Representative mechanical data for selected experiments are presented in Figure 1. At effective pressure up to 20 MPa, the mechanical response and failure mode were typical of the brittle faulting regime. The differential stress ($\sigma_1 - \sigma_3$) attained a peak, beyond which strain softening was observed (Fig. 1a). The peak stress showed a positive correlation with the confining pressure and effective mean stress (Fig. 2), and macroscopic shear bands oriented at $\sim 30°$ with respect to the σ_1 direction were observed in the failed samples. Whereas dilatancy initiated before the stress peak was attained at 5 MPa of effective pressure, continuous compaction was observed beyond about 20 MPa of effective pressure (Fig. 1b).

At effective pressure $P_{\text{eff}} \geq 40$ MPa, visual examination of the failed samples did not discern features that would suggest localized failure. All the samples showed

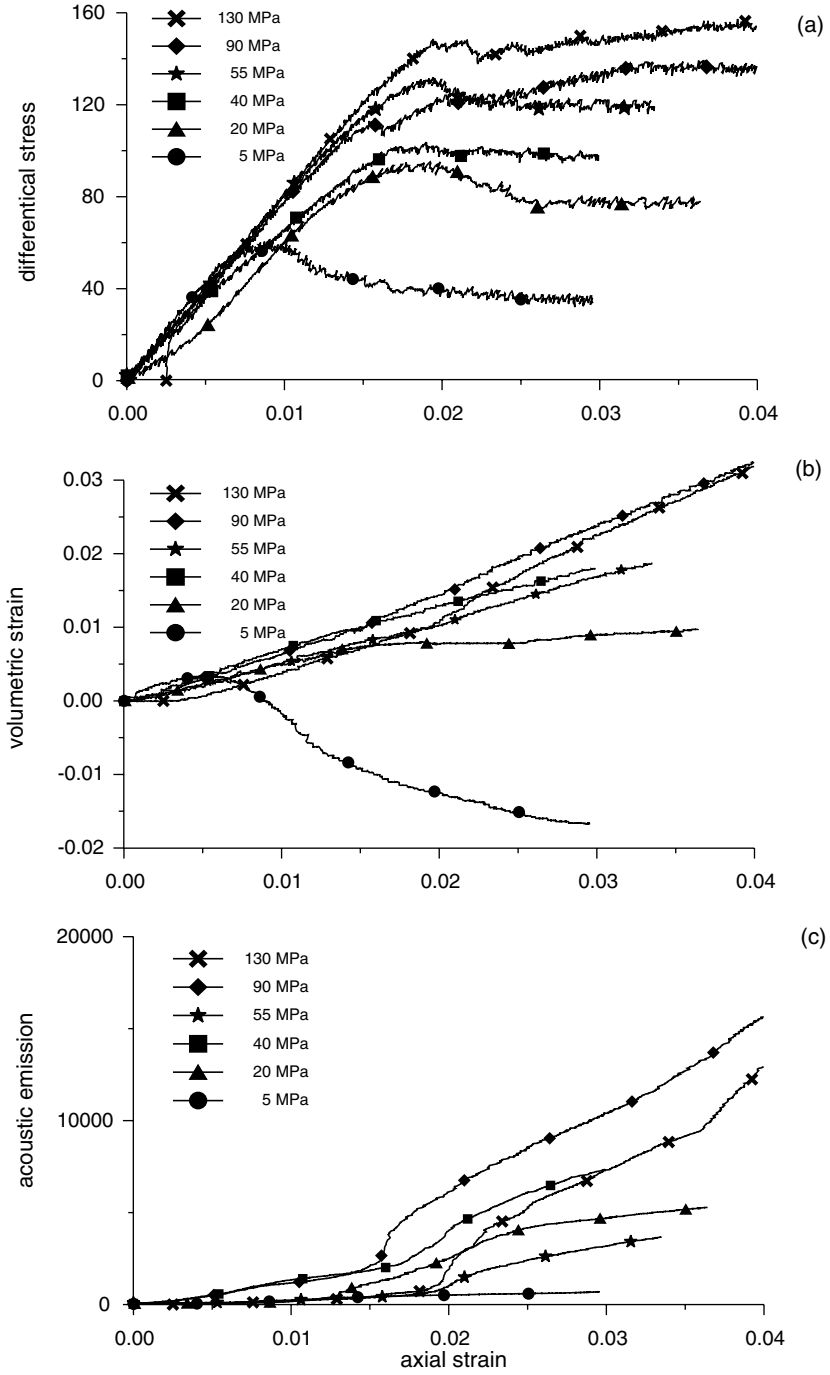

Figure 1
Mechanical data : Differential stress (a), volume strain (b) and acoustic emission (c) versus axial strain for effective pressure between 5 and 130 MPa.

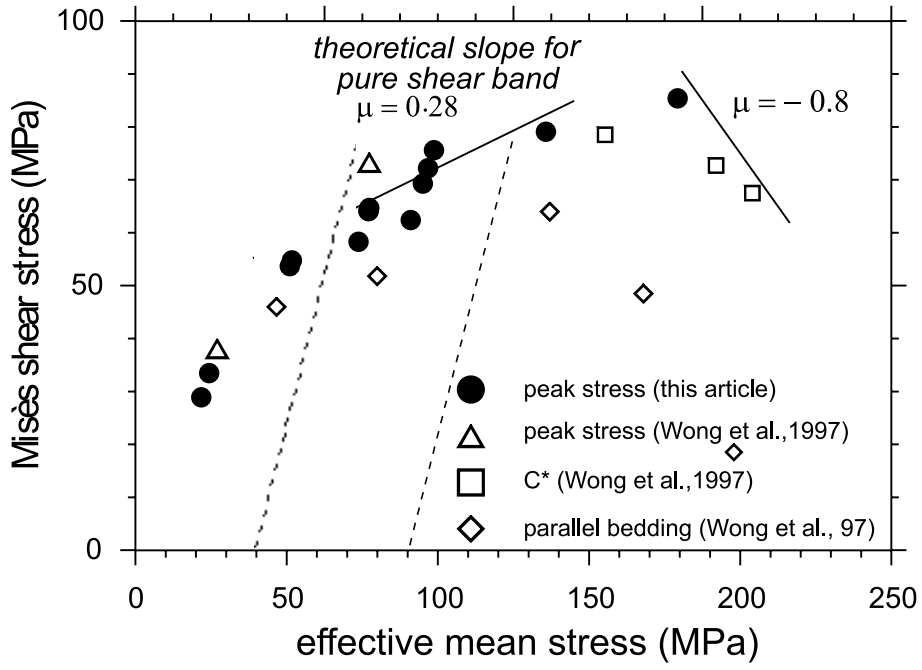

Figure 2
Peak stress and onset of shear enhanced compaction in the Misès shear stress versus effective mean stress plane. μ denotes the friction coefficient.

shear-enhanced compaction (CURRAN and CARROLL, 1979) that initiated at a stress level C^*, beyond which there was an accelerated decrease in volume in comparison to the hydrostat (Fig. 1b). A peak stress followed by a small amount of strain softening was still observed in most of the samples (Fig. 1a). A surge in acoustic emission activity was commonly observed beyond C^* (Fig. 1c).

We compiled the yield stress data in Figure 2. The equivalent Misès shear stress and effective mean stresses for a compressive axisymmetric stress state are defined by $(\sigma_1 - \sigma_3)/\sqrt{3}$ and $(\sigma_1 + 2\sigma_3) - P_p$, respectively. Our data (solid circles) correspond to the peak stresses at effective pressures between 5 and 130 MPa. Data of WONG *et al.* (1997) for the brittle strength and stresses at the onset of shear-enhanced compaction are also included. In the transitional regime (corresponding to effective pressures between 45 MPa and 130 MPa) dilatancy was inhibited even though the differential stress attained a peak. Duplicate experiments indicate appreciable variability in the peak stresses in the transitional regime, which is possibly due to local variations of the bedding direction in our sample block. The sensitivity of strength and yield stress to bedding was documented by WONG *et al.* (1997), who showed that samples cored parallel to bedding (open diamonds in Fig. 2) had significantly lower strengths and yield stresses.

4. Spatial Pattern of Strain Localization—CT Analysis

Altogether twelve deformed samples were prepared for CT imaging. Zones with higher attenuation coefficients are shown in lighter color. For all the specimens analyzed, a number of sub-parallel planar zones with somewhat higher attenuation than the average were observed (Fig. 3). These zones are almost perpendicular to the axial direction and probably associated with the natural sedimentary bedding. In a homogeneous material the brighter zones would correspond to denser materials. However, since the Rothbach sandstone (with modal composition of 68% quartz, 16% feldspar, ~12% clay, and 3% oxides and mica) is by no means monominerallic, the localized anomalies in attenuation may also arise from mineralogical heterogeneity.

At effective pressures of 5 and 20 MPa, the development of dilating shear bands was manifested as inclined planar zones of darker color in the CT images (Figs. 3 and 4). The geometric complexity of these shear bands is illustrated by the images of four circular slices perpendicular to the sample axis (Fig. 4). In each slice several dilatant zones were observed to radiate from an approximately circular zone. The diameter of the concentric zone and spacing between the radial zones both vary with the axial position of the slice.

Although we had expected to observe localized compactant features in samples deformed at effective pressure higher than 40 MPa, our CT images revealed no obvious signs of strain localization. In some specimens a cone of slightly higher density seems to have developed near the ends of the specimens (Fig. 5). Given the low resolution, it is difficult to unambiguously evaluate to what extent these represent strain localization features.

At 130 MPa effective pressure, if present, these localized zones are expected to be at very high angles to the sample axis and almost parallel to the bedding.

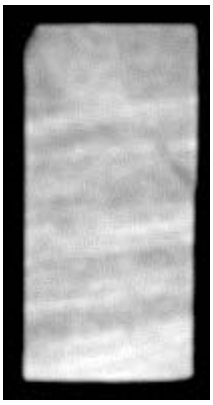

Figure 3
X-ray CT measurement of the whole sample at 20 MPa effective pressure. The imaged plane is parallel to the specimen axis. Shear band are inclined and dilating (darker than the average grey level) and sedimentary bedding is close to perpendicular of the specimen axis.

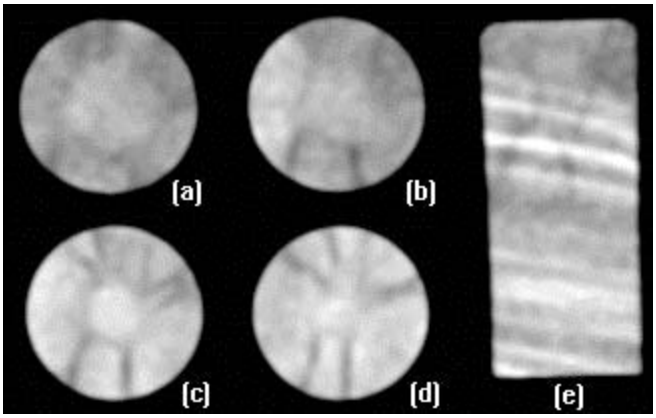

Figure 4
X-ray CT measurements of the whole sample at 5 MPa effective pressure : (a–d) in planes perpendicular to the specimen axis, the size and the spacing out of localisation traces (a circular zone and several radial bands) depend on the position in the specimen; (e) in a vertical mid-section of the specimen, the previous circular zone corresponds to a central V shape and the radial traces to several inclined bands.

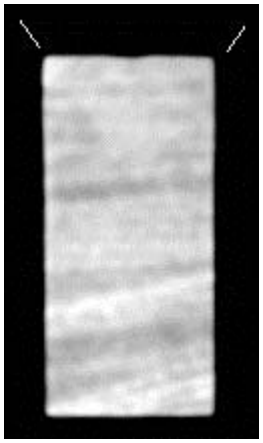

Figure 5
X-ray CT measurements of the whole sample at 55 MPa effective pressure. A cone of compactive strain (slightly brighter than the average grey level) is observed at the top of the specimen.

Consequently it is difficult to differentiate such localized features in a failed sample from the pre-existing bedding heterogeneities.

5. Spatial Evolution of Anisotropic Damage—Microstructural Observation

Microstructural observations were conducted to characterize the spatial distribution of cracking and damage localization in the deformed samples. For reference,

we first studied a sample deformed in the brittle faulting regime at $P_{\text{eff}} = 20$ MPa : sample B1 was deformed to the post-failure stage (to about 3% of axial strain), where the differential stress reached a residual level (Fig. 1a). Shear localization developed from a corner of the sample along a planar zone inclined at an angle of $\sim 40°$ to σ_1 (Figs. 3 and 6). The width of the shear band varied by a factor of ~ 3, with a minimum of $\sim$ 0.5 mm (which is comparable to the average grain diameter of 0.6 mm). Its central part was subject to intense grain crushing. In the periphery of the band extensive inter- and intra-granular cracking occurred. Crack density decreased quickly and transversely to the band. Beyond a distance of 4 or 5 grains, damage became very slight. A few intra-granular cracks preferentially aligned in an approximately axial direction were observed in grains neighboring the shear zone (Fig. 7). Damage anisotropy in Rothbach sandstone is qualitatively similar to what was observed in Berea sandstone (21% porosity) by MENÉNDEZ *et al.* (1996).

Stereological measurements were performed on four samples deformed in the transitional regime at effective pressures 40, 55, 90 and 130 MPa. Using equation (1) the crack surface area per unit volume (S_v) was inferred from linear intercept measurements along two orthogonal directions. The samples deformed at 40 and 55 MPa effective pressures showed similar spatial distributions of damage (Fig. 8). In

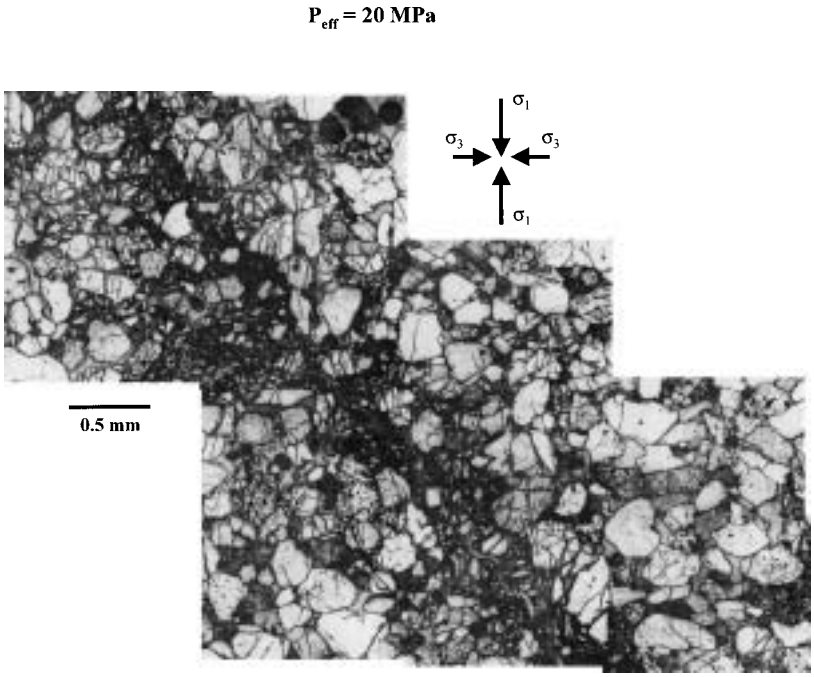

Figure 6
Mosaic of optical (reflexion) micrographs showing part of the shear band that developed in sample B_1 deformed in the brittle regime.

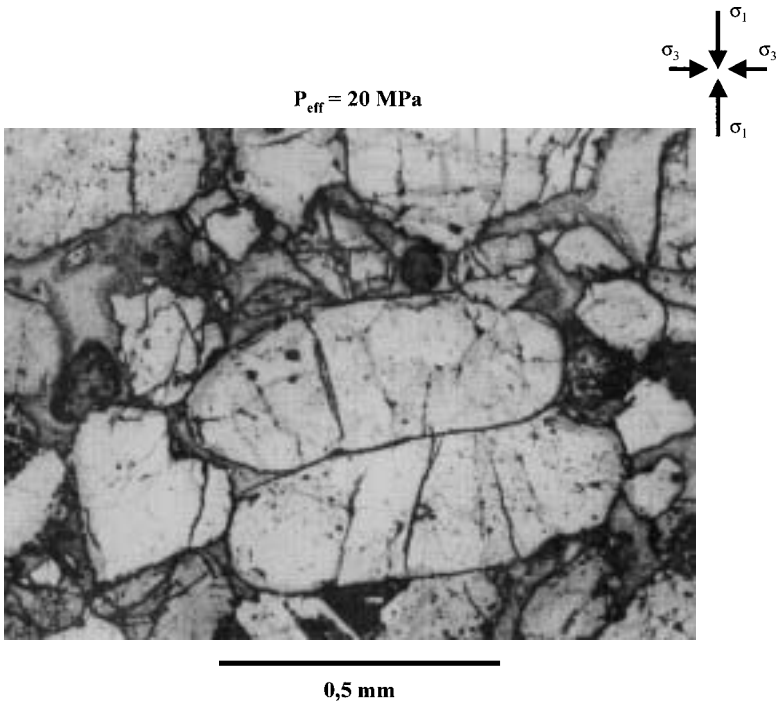

Figure 7
Intragranular cracks outside the shear band in sample B_1 deformed in the brittle regime.

all cases damage affected near one or both ends of the sample, and the cumulative area of the localized zones did not exceed 1/3 of the total surface of the sample. Within the high damage areas, the crack density is higher than the background by as much as a factor of 5. For example, we found in sample T_2 an average of 4.3 m^{-1} for S_v and a maximum of 14.6 m^{-1}. These values are in the range found by MENÉNDEZ *et al.* (1996) in shear compacted samples of Berea sandstone. Qualitatively similar distributions of damage were observed in samples T_2 and T_3 from two experiments conducted at effective pressure 55 MPa. High-angle conjugate zones initiated from the sample corners and intersected at a sub-horizontal tabular zone of variable length, where maximum crack density was measured in most cases. In sample T_2 deformed at 55 MPa effective pressure, the length of this tubular zone was ~4 mm. The thin section T_3 was taken from the sample shown in Figure 5. Locations of the high-angle conjugate zones in the thin section roughly correspond to those where an axi-symmetric compacting cone was vaguely resolved by CT.

In Figure 9, we present micrographs corresponding to different areas of sample T_3 (deformed to 3% of axial strain). Intensive grain crushing occured in the upper part of the sample (Figure 9a). Numerous "Hertzian fractures" radiating from grain contacts (MENÉNDEZ *et al.*, 1996; WU *et al.*, 1999) were observed. The damage

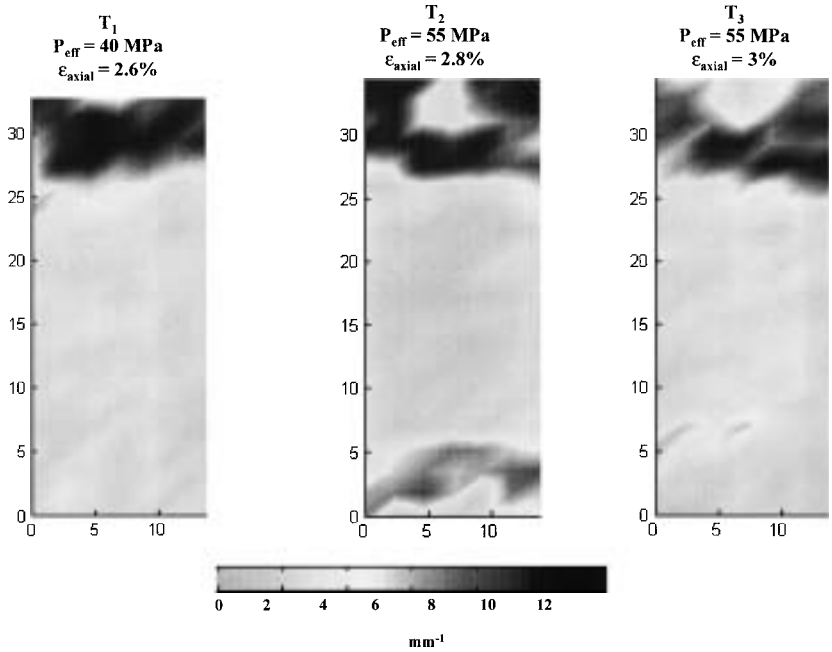

Figure 8
Spatial distribution of specific surface area in sample T_1 deformed at $P_{eff} = 40$ MPa (a), and in samples T_2 (b) and T_3 (c) deformed at $P_{eff} = 55$ MPa. The σ_1 direction is vertical.

anisotropy (evaluated using equation 2) was negligible in this sample, with $\Omega_{23} = 0.1$ within the localized zone and an average value ~ 0 in the whole sample. In Figure 9b pore collapse was evident, and part of the pore space was filled with comminuted particles. This suggests an overall decrease of the porosity in the damaged part of the sample. Figures 9c and 9d depict two different regions of the sample that did not have intensive cracking. Minor damage was in fact observed in both areas, and some of the visible cracks were likely to be present prior to deformation. Figures 9c and 9d show the strong heterogeneity in grain size and porosity that is typical for different layers of the bedding in Rothbach sandstone. Bedding layers were found in most of the thin sections, except in the damaged zones where grain crushing "homogenized" the material. It is therefore unclear, at this point, if the bedding heterogeneity promotes or inhibits damage localization.

At 90 MPa effective pressure (Fig. 10), intensive cracking was observed in a larger portion of the sample (about 1/2), at both ends. The highest crack densities ($S_v = 14.6\,\mathrm{mm}^{-1}$) were measured in association with grain crushing and pore collapse (Fig. 10b). In this area we found an anisotropy factor of about 0.1. In other regions, mostly close to the periphery of the damaged area, subvertical cracking was dominant (Fig. 10c). We consistently measured a maximum of $\Omega_{23} = 0.4$ in these zones. In the central part of the sample, significant differences

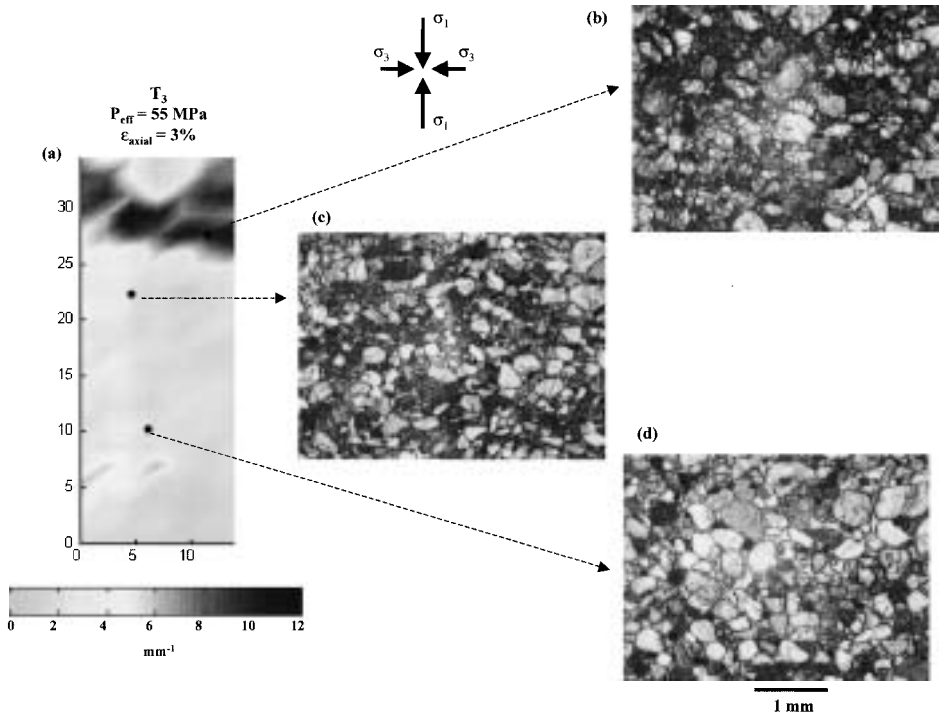

Figure 9
(a) Spatial distribution of specific surface area in sample T_3 deformed at $P_{\text{eff}} = 55$ MPa. (b) Extensive grain crushing where crack density is high. (c) No damage in a compact layer of the sample. (d) No damage in a more porous layer of the sample.

in porosity could be observed (Figs. 10d and 10e). Axial cracking such as observed in Figure 10c appeared to be predominant in the less compact layers of the sample.

At 130 MPa effective pressure, damage was spatially distributed in a clearly different way (Fig. 11). Intensive cracking was observed in about 2/3 of the sample, including the central area. Several localized and elongated clusters were identified (Fig. 11a). In all of them, grain crushing was evident (Fig. 11b). The orientations of these clusters were mainly sub-horizontal (perpendicular to σ_1), and the crack surface area reached a maximum of $S_v = 15.3\,\text{mm}^{-1}$. These localized structures can be interpreted as compaction bands or compacting shear bands at a relatively high angle of $\sim 80°$ degrees with respect to the axial direction. As they are almost parallel to the bedding, it may have been difficult to resolve them in the CT images. We found a relatively low anisotropy factor of $\Omega_{23} = 0.02$ in these compaction bands. Damage level was appreciably less in grains outside the compaction bands (Fig. 11c) and the overall spatial distribution of damage remained anisotropic even at high effective pressure (Fig. 11d).

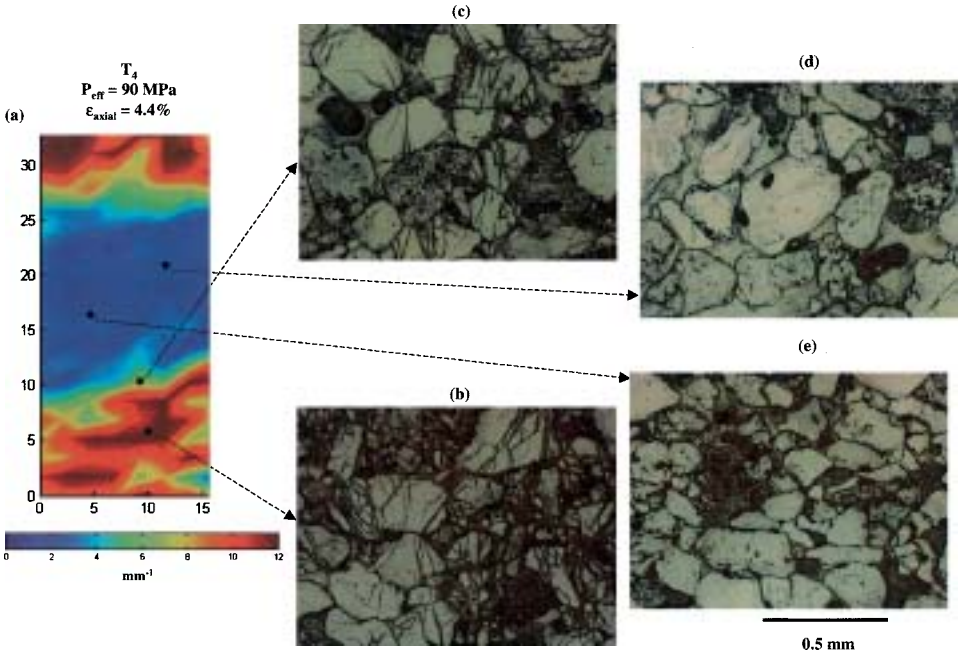

Figure 10
(a) Spatial distribution of specific surface area in sample T_4 deformed at $P_{eff} = 90$ MPa. (b) Extensive grain crushing in a localized cluster of intense damage. (c) Area where axial cracking is dominant. (d) No damage in a compact layer of the sample. (e) No damage in a more porous layer of the sample. The σ_1 direction is vertical.

6. Discussion and Conclusion

6.1. Strain Localization and Failure Mode in the Brittle-Ductile Transition

Our data on the Rothbach sandstone are in qualitative agreement with recent studies by OLSSON (1999) and WONG *et al.* (2001) who have documented the development of high-angle shear bands and compaction bands in sandstones with porosities ranging from 13% to 28%. The localized failure modes are associated with stress states in the transitional regime from brittle faulting to compactive cataclastic flow. These laboratory results suggest that such complex features can be pervasive in sandstone formations, not just in the very porous aeolian sandstone in which they were first documented (MOLLEMA and ANTONELLINI, 1996). Recognition of such structures in the field would elucidate the complex development of localization in sandstone formations (AYDIN and JOHNSON, 1978) and accretionary prisms (BYRNE *et al.*, 1993).

Our microstructural observations and stereological data underscore the spatial heterogeneity of damage associated with the development of high-angle shear and

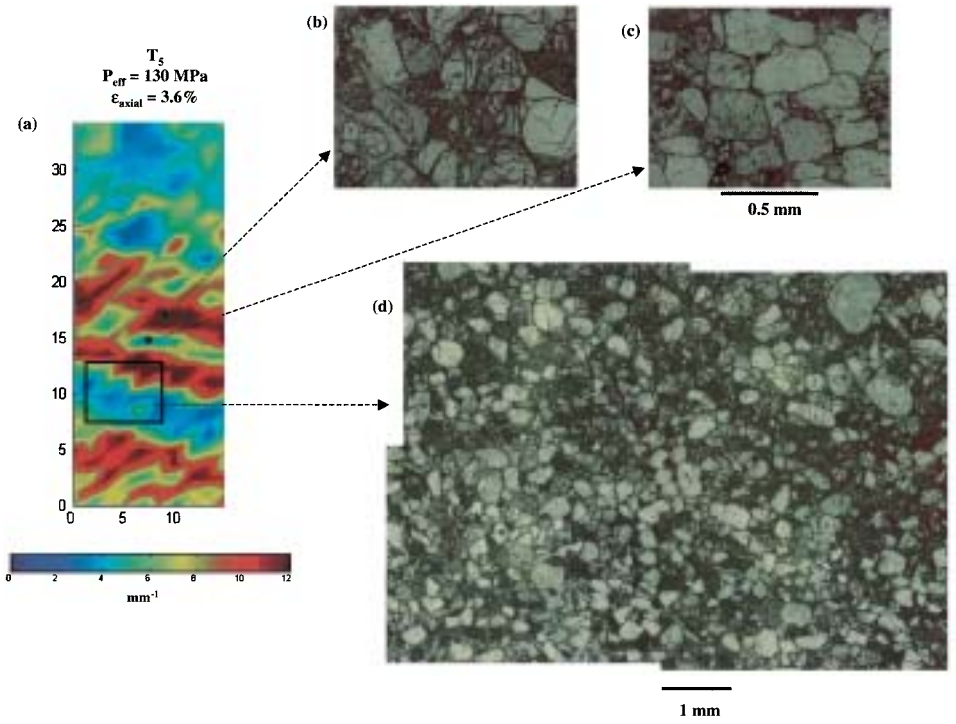

Figure 11
(a) Spatial distribution of specific surface area in sample T_5 deformed at P_{eff} = 130 MPa. (b) Detail of grain crushing in a compaction band. (c) No damage in an area between two compaction bands. (d) Mosaic of micrographs showing the transition between a compaction band and an undamaged zone. The σ_1 direction is vertical.

compaction bands. In the localized bands intensive grain crushing and pore collapse were observed. Similar micromechanical processes were documented by DiGiovanni *et al.* (2000) in laboratory deformed Castlegate sandstone and by Mollema and Antonellini (1996) in naturally deformed Navajo sandstone. Previous laboratory data show that bedding in Rothbach sandstone has significant influence on the failure and yield behavior. Our microstructural observations presented here suggest that the development of compaction band is promoted along planar zones parallel to the bedding.

The CT data have provided preliminary images of the three-dimensional geometric complexity associated with strain localization. At 5 MPa effective pressure, a complex pattern of localization was observed (Fig. 4). Axisymmetric loading and frictional constraints at the specimen ends appear to promote the development of such an axisymmetric pattern, and to inhibit the initiation of a single shear band (which is intrinsically a plane-strain mechanism). The pattern we observed is analogous to that in axisymmetrically compressed specimens of Hostun

RF sand, which was studied by DESRUES *et al.* (1996) as a combination of a cone centered on the axis of the specimen and on a set a plane strain mechanism associated with V-shape pairs.

Since compaction bands have an intrinsically axisymmetric geometry, their development should be promoted by axisymmetrical loading if the constitutive parameters attain the critical conditions for inception of such a localization mode. Since the compaction bands that developed at 130 MPa confining pressure were observed in the mid-section of the sample, we believe frictional end-effects to be minimal in our tests. However, the conical shape of the high-angle shear bands at effective pressures between 40 and 55 MPa may have been influenced by stress heterogeneity from frictional constraints, since they initiated in the proximity of the specimen ends.

6.2. Comparison with Localization Analysis

Bifurcation analyses (RUDNICKI and RICE, 1975; OLSSON, 1999; ISSEN and RUDNICKI, 2000; BÉSUELLE, 2001) specify the mechanical conditions under which such localized failure modes may develop. The simplest approach is to adopt a constitutive framework (RUDNICKI and RICE, 1975) whereby the yield envelope and inelastic volumetric change can be characterized by the pressure-sensitivity parameter μ and dilatancy factor β, respectively. The parameter μ can be inferred from the slope of the yield stress data as indicated in Figure 2. Our data together with those of WONG *et al.* (1997) for samples cored perpendicular to the bedding indicate that $-0.8 \leq \mu \leq 0.28$ in the transitional regime. For this range of μ values and Poisson ratio equal to 0.14 (inferred from our laboratory data), the bifurcation analyses predict that localized failure occurs by three possible modes :

1. A *pure shear* band (with negligible volumetric change throughout the sample) may develop for an associated model (i.e., $\mu = \beta$) for $\mu = 0.28$ (BÉSUELLE, 2001).
2. A *compaction* band perpendicular to σ_1 may develop for negative values of μ and β such that $\beta + \mu < -\sqrt{3}$ (ISSEN and RUDNICKI, 2000).
3. A *compacting shear* band at high angle may develop for intermediate values of μ and β such that $\beta + \mu \geq -\sqrt{3}$.

WONG *et al.* (2001) recently showed that the dilatancy factors for Bentheim, Berea and Darley Dale sandstones (deformed in the brittle-ductile transitional regime) fall in the range $-\sqrt{3}/2 < \beta < 0$. They argued that these limiting values arise from the plastic strain field in this regime which is characterized by axial shortening (probably dominated by pore collapse) and lateral expansion (probably induced by axial microcracking). Values of β for Rothbach sandstone in the transitional regime are expected to also fall within these limits, which imply that $\beta + \mu \geq -(\sqrt{3}/2 + 0.8) > -\sqrt{3}$. Accordingly, the bifurcation analysis would rule out the possibility of compaction band formation (mode 2) and predict the development of localization by

either mode 1 or mode 3. These two localization modes correspond to the mosaics of high-angle shear bands revealed in our microstructural observations of samples deformed at effective pressures less than 130 MPa (Figs. 8–10). The bifurcation analysis also predicts that such localization modes develop during the strain softening stage (Fig. 1). To explore this further we should conduct observations on samples deformed to different stages to study the progressive development of localization.

Moreover, the bifurcation analysis (BÉSUELLE, 2001) predicts the development of dilating shear bands during the post-peak stage for $\mu > 0.28$ (if $\beta \approx \mu$). Constitutive parameters for Rothbach sandstone deformed at effective pressures of 5 MPa and 20 MPa satisfy these conditions. Our CT and microstructural observations indicate that the localized bands developed as dilating shear bands.

However, there is an apparent discrepancy in that our microstructural observations indicate formation of compaction bands in the sample failed at the effective pressure of 130 MPa (Fig. 11), even though the bifurcation analysis rules out this localization mode (mode 2). The discrepancy may arise from several intrinsic limitations in the constitutive framework of RUDNICKI and RICE (1975) that was adopted in the localization analyses. First, the plastic yield behavior is assumed to be isotropic, even though the mechanical data for Rothbach sandstone (WONG *et al.*, 1997; MILLIEN, 1993) and our microstructrual observations both indicate significant anisotropy due to the sedimentary bedding. RUDNICKI's (1977) theoretical analysis has shown that the onset of localization is sensitive to mechanical anisotropy. Second, the constitutive model does not adequately account for plastic yield and volume change induced by the mean stress (AYDIN and JOHNSON, 1983). ISSEN and RUDNICKI (2000) recently proposed a constitutive model that incorporates multiple yield surfaces and damage mechanisms, with predictions on compaction band formation that seem to be in better agreement with laboratory and microstructural observations (WONG *et al.*, 2001). More systematic studies are necessary before we can make quantitative comparisons with such a more elaborate model.

Acknowledgements

We are grateful to Maurice Boutéca who allowed us to use the X-ray apparatus at the Institut Français du Pétrole and to Camille Schlitter who performed the measurements. We thank Yves Guéguen who stimulated this work. We have benefited from discussions with John Rudnicki and Kathleen Issen. The research programs at Paris and Stony Brook were partially supported by joint program Centre National de la Recherche Scientifique (CNRS) and National Sciences Foundation (NSF) under grants EAR9805072, EAR0006932 and INT9815570.

REFERENCES

ANTONELLINI, M., AYDIN, A., POLLARD, D. D., and D'ONFRO, P. (1994), *Petrophysical Study of Faults in Sandstone Using Petrographic Image Analysis and X-Ray Computerized Tomography*, Pure Appl. Geophys. *143*, 181–201.

AYDIN, A. and JOHNSON, A. M. (1978), *Development of Faults as Zones of Deformation Bands and as Slip Surfaces in Sandstone*, Pure Appl. Geophys. *116*, 931–942.

AYDIN, A. and JOHNSON, A. M. (1983), *Analysis of Faulting in Porous Sandstones*, J. Struct. Geol. *5*, 19–31.

BAUD, P., ZHU, W., and WONG, T.-f. (2000), *Failure Mode and Weakening Effect of Water on Sandstone*, J. Geophys. Res. *105*, 16371–16389.

BÉSUELLE, P. (2001), *Compacting and Dilating Shear Bands in Porous Rocks: Theoretical and Experimental Conditions*, J. Geophys. Res., 106, 13435–13442.

BÉSUELLE, P., DESRUES, J., and RAYNAUD, S. (2000), *Experimental Characterisation of the Localisation Phenomenon Inside a Vosges Sandstone in a Triaxial Cell*, Int. J. Rock Mech. Min. Sci. *37*, 1223–1237.

BYRNE, T., MALTMAN, A., STEPHENSON, E., SOH, W., and KNIPE, R. (1993), *Deformation Structures and Fluid Flow in the Toe Region of the Nankai Accretionary Prism*, Proc. of the ODP, Scientific Results *131*, 83–192.

CURRAN, J. H. and CARROLL, M. M. (1979), *Shear Stress Enhancement of Void Compaction*, J. Geophys. Res. *84*, 1105–1112.

DAVID, C., WONG T.-f., ZHU, W., and ZHANG, J. (1994), *Laboratory Measurement of Compaction-Induced Permeability Change in Porous Rock: Implications For the Generation and Maintenance of Pore Pressure Excess in the Crust*, Pure Appl. Geophys. *143*, 425–456.

DESRUES, J., CHAMBON, R., MOKNI, M., and MAZEROLLE, F. (1996), *Void Ratio Evolution Inside Shear Bands in Triaxial Sand Specimens Studied by Computed Tomography*, Géotechnique *46*, 529–546.

DIGIOVANNI, A. A., FREDRICH, J. T., HOLCOMB, D. J., and OLSSON, W. A. (2000), *Micromechanics of Compaction in an Analogue Reservoir Sandstone*, Proc. 4th North Am. Rock Mech. Symp. 1153–1160.

ISSEN, K. A. and RUDNICKI, R. J. (2000), *Conditions for Compaction Bands in Porous Rock*, J. Geophys. Res. *105*, 21529–21536.

KAWAKATA, H., CHO, A., KIYAMA, T., YANAGIDANI, T., KUSUNOSE, K., and SHIMADA, M. (1999), *Three-dimensional Observations of Faulting Process in Westerly Granite Under Uniaxial and Triaxial Conditions by X-Ray CT Scan*, Tectonophysics *313*, 293–305.

LABUZ, J. F. and BRIDEL, J. M. (1993), *Reducing Frictional Constraint in Compression Testing through Lubrication*, Int. J. Rock Mech. Min. Sci. *20*, 451–455.

MENÉNDEZ, B. ZHU, W., and WONG, T.-f. (1996), *Micromechanics of Brittle Faulting and Cataclastic Flow in Berea Sandstone*, J. Struct. Geol. *18*, 1–16.

MILLIEN, A. (1993), *Comportement anisotrope du grès des Vosges: élasto-plasticité, localisation, rupture*, Ph.D. Thesis, Univ. of Grenoble, Grenoble, France, 220 pp.

MOLLEMA, P. N. and ANTONELLINI, M. A. (1996), *Compaction Bands: A Structural Analog For Anti-Mode I Cracks in Aeolian Sandstone*, Tectonophysics *267*, 209–228.

OLSSON, W. A. (1999), *Theoretical and Experimental Investigation of Compaction Bands in Porous Rock*, J. Geophys. Res. *104*, 7219–7228.

OLSSON, W. A. and HOLCOMB, D. J. (2000), *Compaction Localization in Porous Rock*, Geophys. Res. Lett. *27*, 3537–3540.

PATERSON, M. S., *Experimental Rock Deformation-The Brittle Field* (Spinger-Verlag, New York 1978).

RAYNAUD, S., FABRE, D., MAZEROLLE, F., GERAUD, Y., and LATIERE, H. J. (1989), *Analysis of the Internal Structure of Rocks and Characterization of Mechanical Deformation by a Non-destructive Method: X-ray Tomodensitometry*, Tectonophysics *159*, 149–159.

RUDNICKI, J. W. (1977), *The effect of stress-induced anisotropy on a model of brittle rock failure as localization of deformation*. In *Energy Resources and Excavation Technology*, Proc. 18th U.S. Symp. on Rock Mechanics, pp. 1–8, Keystone, Colorado.

RUDNICKI, J. W. and RICE, J. R. (1975), *Conditions for the Localization of Deformation in Pressure Sensitive Dilatant Materials*, J. Mech. Phys. Solids *23*, 371–394.

UNDERWOOD, E. E., *Quantitative Stereology* (Addison Wesley, Reading 1970).

VINEGAR, H. J., DE WAAL, J. A., and WELLINGTON, S. L. (1991), *CT Studies of Brittle Failure in Castlegate Sandstone*, Int. J. Rock Mech. Min. Sci. *28*, 441–448.

WELLINGTON, S. L. and VINEGAR, H. J. (1987), *X-Ray Computerized Tomography*, J. Pet. Tech. *39*, 885–898.

WONG, T.-f., DAVID, C., and ZHU, W. (1997), *The Transition From Brittle Faulting To Cataclastic Flow in Porous Sandstones: Mechanical Deformation*, J. Geophys. Res. *102*, 3009–3025.

WONG, T.-f., BAUD, P., and KLEIN, E. (2001), *Localised Failure Modes in a Compactant Porous Rock*, Geophys. Res. Lett., *28*, 2521–2524.

WU, X. Y., BAUD, P., and WONG, T.-f. (1999), *Micromechanics of Compressive Failure and Spatial Evolution of Anisotropic Damage in Darley Dale Sandstone*, Int. J. Rock Mech. Min. Sci. *37*, 1–18.

(Received March 7, 2001, revised June 1, 2001, accepted August 1, 2001)